

SMASIS2019-5565

MULTIFUNCTIONAL STRUCTURES FOR ATTITUDE CONTROL

Vedant

University of Illinois at Urbana-Champaign
Aerospace Engineering
Urbana, IL 61801
Email: vedant2@illinois.edu

James T. Allison

University of Illinois at Urbana-Champaign
Industrial & Enterprise Systems Engineering
Aerospace Engineering
Urbana, IL 61801
Email: jtalliso@illinois.edu

ABSTRACT

The Engineering Systems Design Lab (ESDL) at the University of Illinois introduced Strain-Actuated Solar Arrays (SASAs) as a solution for precise satellite Attitude Control System (ACSs). SASA is designed to provide active mechanical vibration (jitter) cancellation, as well as small slew maneuver capabilities to hold a pose for short time periods. Current SASA implementations utilize piezoelectric distributed actuators to strain deployable structures, and the resulting momentum transfer rotates the spacecraft bus. A core disadvantage, however, is small strain and slew capability. Initial SASA systems could help improve pointing accuracy, but must be coupled with another ACS technology to produce large reorientations. A novel extension of the original SASA system is presented here that overcomes the small-displacement limitation, enabling use of SASA as a sole ACS for some missions, or in conjunction with other ACSs. This extension, known as Multifunctional Structures for Attitude Control (MSAC), can produce arbitrarily-large rotations, and has the potential to scale to large spacecraft. The system utilizes existing flexible deployable structures (such as solar arrays or radiators) as multifunctional devices. This multi-role use of solar panels extends their utility at a low mass penalty, while increasing reliability of the spacecraft ACS.

1 Introduction

Spacecraft attitude control is the process of orienting a satellite toward a particular point in the sky, precisely and accurately. Attitude control of a spacecraft enables proper function in space. For instance, orienting solar panels toward the sun or orienting a science payload, such as imagers/cameras, toward objects of

interest. The precision of spacecraft attitude control is critical for many space observatory and optics-based payloads. Satellite pointing precision is quantified using the metric ‘pointing accuracy’. Pointing Accuracy measures the uncertainty of the pointing of an instrument along a selected direction based on vector measurements to a set of known beacons, such as stars, ground, or space objects. Different science payloads have demanded different levels of pointing accuracy, with optical imaging payloads demanding accuracy up to the nano-radian (milliarcsecond) scale [1]. Multiple new space telescopes are being designed with unprecedented levels of required pointing accuracy [2–4], motivating the development of new ACS technologies with enhanced accuracy (while maintaining or improving reliability).

Attitude control for satellites has been achieved using a range of established attitude control actuators, such as reaction thrusters, magnetic torque coils, and momentum management devices [5]. Reaction Wheel Assemblies (RWAs), Control Moment Gyroscopes (CMGs), and nutation dampers are examples of moment management devices, which produce attitude changes without applying any external torques, and hence causing no change in net angular momentum. Instead, momentum exchange devices rotate satellites by temporarily altering the distribution of angular momentum between devices and the rest of the spacecraft. These alterations can then produce a secular change in attitude. Conventional satellites utilize RWAs or CMGs for arbitrarily-large attitude control maneuvers, coupled with vibration isolation systems, to achieve the required performance. Several space science mission lifespans have been shortened due to a malfunction of the Attitude Control System (ACS), resulting in an inability to provide the pointing required by the science pay-

load [6]. Reliability problems and vibration from high-speed rotating components motivate investigation of new ACS strategies with potential for quieter and more reliable operation.

The Strain-Actuated Solar Array (SASA) ACS is a recently-introduced solution for cancellation of mechanical vibration (jitter), and for producing small slew maneuvers that hold a pose for short time periods. The SASA system utilizes deployable spacecraft panels as multifunctional structures. These panels provide precise, but limited (small angle), attitude control in addition to their primary functions. Current SASA implementations utilize distributed piezoelectric actuators to strain the deployable structures, and the resulting momentum transfer rotates the spacecraft bus [7, 8]. The system has been studied using co-design methods to identify system-optimal distributed structure and control designs [8, 9]. These monolithic actuators have the advantage of inherently improved reliability compared to conventional ACSs (sliding contact is eliminated), as well as high-bandwidth actuation. A core disadvantage, however, is a small strain and slew capability. Initial SASA systems helped improve pointing accuracy, but must be coupled with other ACS technologies to produce large reorientations. Also, similar to most momentum exchange devices, SASA cannot provide momentum dumping functionality.

A novel extension of the original SASA system is presented here that overcomes the small-displacement limitation, enabling use of SASA as an independent ACS for some missions. This extension, known as Multifunctional Structures for Attitude Control (MSAC), can produce arbitrarily-large rotations and has the potential to scale to large spacecraft. Some older concepts of similar nature have been demonstrated using geometric control theory [10, 11], but they rely on robotic appendages with sliding contacts to produce attitude maneuvers. The MSAC concept produces similar motions without the use of any sliding contacts, thereby eliminating the need for sliding mechanical contacts (traditional joints), and their associated failure models.

The article first discusses the principle of operation that MSAC utilizes, a preliminary analysis of system performance is developed. Then, the Finite Element Analysis (FEA) of different actuators that can be used with deployable panels to achieve the desired motion is presented. Subsequently, a reduced-order model based on a multibody simulation is used to approximate system dynamics both for control and design purposes.

2 Motivation

Momentum exchange devices are one of the most widely-used attitude control actuators for standard satellites. Most satellites use moment exchange devices such as RWAs [12] and CMGs, coupled with magnetic torque coils or reaction control thrusters [5]. Thrusters and torque coils involve forces external to the satellite, allowing RWAs or CMGs to desaturate (reduce speed). This process is known as momentum dumping, as it al-

lows satellites to shed momentum acquired from unavoidable external forces (such as solar pressure).

RWAs and CMGs both use rotating wheels for attitude control. While these actuators are balanced to very high standards, small imbalances in high-speed rotating components induce mechanical vibration noise (jitter) to the system. This source of jitter is exacerbated as engineers increase rotational speeds to improve control authority. To advance the capabilities of scientific payloads, it is desirable to eliminate RWAs and CMGs as jitter sources.

Multiple missions have suffered due to reduced lifespans or have been unsuccessful in achieving their science objectives due to RWA/CMG failures [6]. A primary factor in these failures is the sliding contact present in RWA/CMG bearings. On some missions, ACS systems with redundant wheels have been used to improve reliability. This increases cost, mass, and complexity, and in recent important missions, multiple RWA/CMG failures have resulted in the loss of ACS functionality despite the system redundancy.

SASA can actively cancel the mechanical noise on a satellite platform (e.g., from RWAs/CMGs, cryogenic pumps, or other dynamic components), and the monolithic design of SASA does not involve sliding contacts. PZT actuators are noted for high-reliability. In addition, SASA makes use of existing vehicle mass (deployable panels), so has the potential to reduce overall vehicle mass. Current SASA systems, however, can produce only small angular rotations, so must be combined with additional ACS actuators, such as RWAs/CMGs or thrusters. This article introduces a fundamentally new approach in the design and control of SASA systems that enables arbitrarily-large reorientations, eliminating the need to combine SASA with RWA/CMG actuators. This is an important step toward realizing the goals of simultaneously reducing vehicle mass, improving pointing accuracy, enhancing reliability, and managing cost.

3 System description and concept of operation

The MSAC system utilizes existing deployable structures/appendages (such as solar arrays or radiators) as multifunctional devices. This multi-role use of the solar panels extends their utility at a low mass penalty, while increasing spacecraft ACS reliability. The new design concept presented here adds completely new functionality to SASA systems: execution of arbitrarily-large spacecraft rotations (secular motion) with no sliding contacts in the ACS.

3.1 Concept of operation

To produce secular motion, we propose the utilization of transverse oscillations of the deployable panels *combined* with moment of inertia (MOI) reconfigurations. Both oscillations and reconfigurations are achieved by exercising the same set of dis-

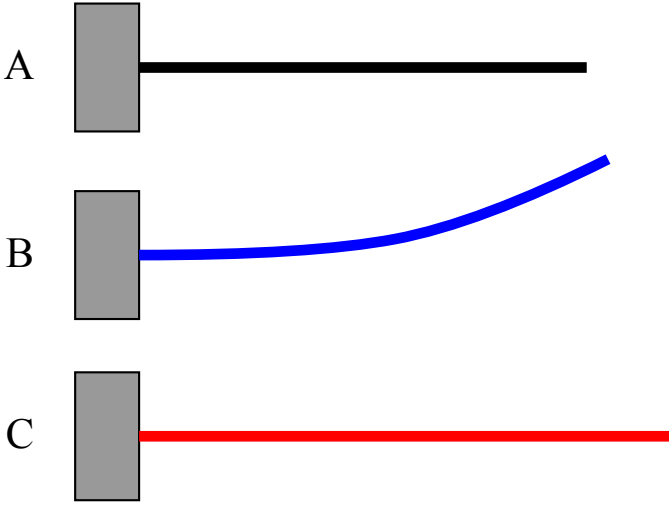


FIGURE 1: An illustration of one possible instantiation of the two types of strain that can produce secular attitude variation using the MSAC design: 1) $A \rightarrow B$ and 2) $A \rightarrow C$

tributed actuators. Strategic adjustments to MOI between transverse oscillations produce a secular change in attitude. One mechanism for changing MOI is to induce longitudinal strains, increasing or decreasing the MOI about the vehicle axis of rotation. To illustrate one possible instantiation of the MSAC concept, the two constituent phases are illustrated using a single axis of rotation MSAC system as follows:

1. Strain deployable structures for jitter control or for producing small slew maneuvers in the transverse panel direction. This is illustrated in Fig. 1, straining from the elastic equilibrium position (A) to the displaced position (B).
2. Strain deployable structures to alter inertial properties, seen in Fig. 1, straining from rest (A) to (C).

The latter element is a nonlinear behavior that allows the ACS to ‘reset’ between movements, producing secular variation in attitude. From a dynamical system perspective, MSAC utilizes trajectories that are non-holonomic. A more detailed description of the non-holonomic trajectory is presented next, using lumped models to simplify the discussion.

3.2 Performance of an illustrative simplified system

The analysis in this section assumes that the system utilizes lumped actuators to alter MOI to produce the motion. Actual implementations of monolithic MSAC systems would use distributed actuation and infinite Degrees of Freedom (DOFs) in the deployable structure. The simplified example presented here for illustrating the MSAC concept of operation involves a single translational DOF, represented as a prismatic joint, to alter the length of a panel (a possible way to modify the MOI). Extension and contraction of the panel are resisted by an elastic

restoring force, tending to bring the panel to a rest length (I_{rest}). This example system also uses a single rotational DOF to rotate the panels relative to the spacecraft body. The panels are assumed to be rigid, and these two DOFs are an approximation of the distributed panel bending and extension shown in Fig. 1. The core strategy using bending (momentum transfer) and extension/contraction (MOI adjustment) to produce secular rotation is illustrated in Fig. 2. This simplified example supports the discussion of an attitude control maneuver about a single axis. While this is a simplified planar case, the MSAC concept extends to full three-axis maneuvers *without loss of generality*. The richer physics (e.g., dynamic coupling) in the three-axis case supports more sophisticated maneuver possibilities.

Assume that the MOI of the satellite body is I_{sat} , and that the MOI of the deployable panel at its rest length (equilibrium—neither contracted nor extended) is I_{rest} . Since the linear prismatic joint can extend and contract the panel, the panel inertia I_{rest} may be adjusted within the range between I_e (extension) and I_c (contraction), where these values correspond to the longest and shortest allowable panel lengths, respectively. To produce secular motion the panel needs to bend about the rotational DOF in a direction (e.g., clockwise) while in extension, and then in the opposite direction (counter-clockwise) while in contraction to produce a net rotation in the first direction. The complete process involves four phases, and is illustrated in Fig. 2 shows the four distinct phases in the trajectory to produce the attitude maneuver. This process may be repeated to produce rotations of any desired angle within the precision capabilities of the MSAC system.

The following analysis assumes that the initial clockwise motion (Fig. 2, Phase I to Phase II) through angle $\theta_a + \theta_b$ requires t_{be} seconds, the anti-clockwise motion (Fig. 2, Phase III to Phase IV) requires t_{bc} seconds, and that the prismatic motion (Fig. 2, Phase II to Phase III and Phase IV to the dashed outline in Phase I) is considerably faster than the rotational motion, i.e., $t_{be}, t_{bc} \gg t_e, t_c$. The angular displacement magnitude of the satellite at Phases II and III from the Phase I orientation is θ_β , and the total net rotation of the satellite at the end of the process is θ_γ .

During the rotational motion, utilizing conservation of angular momentum, we can describe the motion of the system using Eqn. (1):

$$I_{\text{sat}}\omega_{\text{sat}} + I_e\omega_{\text{panel}} = 0 \quad (1a)$$

$$I_{\text{sat}}\omega_{\text{sat}} + I_c\omega_{\text{panel}} = 0 \quad (1b)$$

With these assumptions we can integrate Eqn. (1), and with simplification the result is shown in Eqn. (2):

$$\int_0^{t_{be}} I_{\text{sat}}\omega_{\text{sat}} dt = - \int_0^{t_{be}} I_e\omega_{\text{panel}} dt \quad (2a)$$

$$I_{\text{sat}} \int_0^{t_{be}} \omega_{\text{sat}} dt = -I_e \int_0^{t_{be}} \omega_{\text{panel}} dt \quad (2b)$$

$$I_{\text{sat}}(\theta_\beta - 0) = I_e(\theta_a - \theta_a) \quad (2c)$$

Similarly, the equation of motion during the panel compression

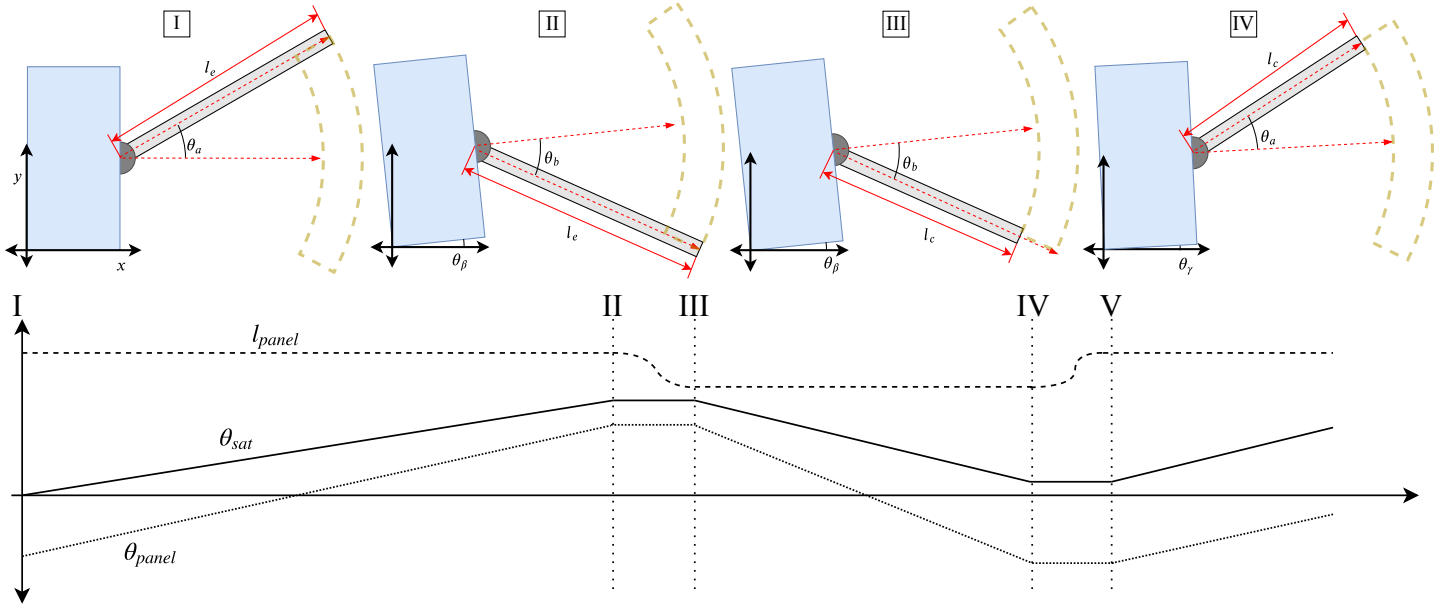


FIGURE 2: MSAC system demonstration with the non-holonomic trajectories (above). The reachable space for the appendage/deployable panel can be seen as the dashed yellow annulus ring sector. The trajectory plot of key state vectors during the different phases is shown in the plot below, with the satellite attitude angle depicted as a solid line, the angle of the panel with respect to the body depicted as a dotted line, and length of the panel as a dashed line. Phase V of the trajectory is shown in Fig. 3.

phase bending can be described by Eqn. (3):

$$I_{sat} \int_{t_{be}}^{t_{be}+t_{bc}} \omega_{sat} dt = -I_c \int_{t_{be}}^{t_{be}+t_{bc}} \omega_{panel} dt \quad (3a)$$

$$I_{sat}(\theta_\gamma - \theta_\beta) = I_c(\theta_b - \theta_a) = -I_c(\theta_a - \theta_b) \quad (3b)$$

The composition of the motions described in Eqn. (2) and Eqn. (3) yields Eqn. (4):

$$I_{sat}(\theta_\gamma - \theta_\beta) + I_{sat}\theta_\beta = I_c(\theta_b - \theta_a) - I_c(\theta_a - \theta_b) \quad (4)$$

Upon simplification,

$$I_{sat}(\theta_\gamma) = (I_e - I_c)(\theta_a - \theta_b), \quad (5)$$

$$\theta_\gamma = \frac{(I_e - I_c)}{I_{sat}}(\theta_a - \theta_b), \quad (6)$$

it can be seen that the satellite body has rotated by a small angle θ_γ , while the panels have been reset back to the same relative orientation with respect to the spacecraft as in Phase I (θ_a). The average angular velocity of the attitude maneuver can be approximated using the following linear approximation:

$$\omega_\gamma \approx \frac{\theta_\gamma}{\Delta t} = \frac{(I_e - I_c)(\theta_a - \theta_b)}{I_{sat}\Delta t}, \quad (7)$$

where $\Delta t = t_{bc} + t_{be} + t_e + t_c$ is the time required to perform one complete cycle (Phase I through Phase IV), as illustrated in Fig. 4.

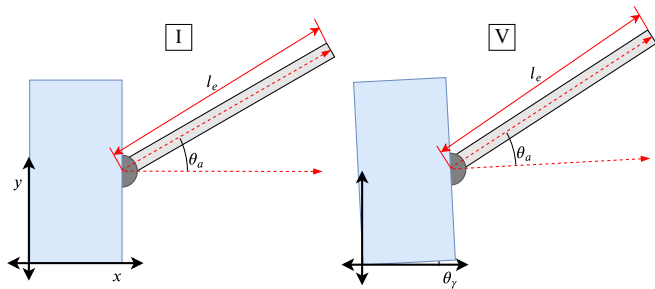


FIGURE 3: Illustration of an attitude maneuver using the MSAC system. Phase I is exactly the same as Phase V, except that the satellite has experienced a net rotation of θ_γ .

4 Results and discussions

This section discusses examples of actuators and mechanisms that could be used to produce the desired motions. The performance of these initial designs is quantified using transient finite element analysis (FEA). Table 1 shows the parameters used to generate the mesh for the two types of actuators discussed, and the resultant number of elements and nodes. The FEA analysis was carried out in SolidWorks, using the available "Nonlinear Dynamic" simulation solvers. The control trajectories produce bending actuation at first, and then transition to extension actuation for each actuator. The simulation initializes with an unstained structure but with the actuators producing a particular force profile.

Properties	Simple Actuator	Amplified actuator
Mesh type	Curvature-based mesh	
Maximum element size	3 mm	
Minimum element size	0.6 mm	
Jacobian calculation	16 points	
Total nodes	64569	16589
Total elements	40494	8480

TABLE 1: Mesh generation parameters for FEA

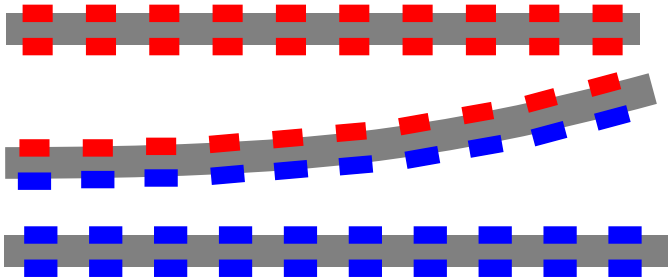


FIGURE 4: Illustration of distributed strain actuators used to produce the contraction, bending, and extension deformations illustrated in Fig. 1. Strain actuators (e.g., piezoelectric patches, electromagnetic coils, etc.) are depicted using small boxes attached to the deployable structure body. Actuators undergoing extension are shown in blue, and those undergoing contraction are shown in red.

4.1 Actuator and mechanisms

To perform the bending and extension/contraction deformations required to achieve secular variation in attitude, actuators and mechanisms are required that produce these deformations while minimizing the risk of failure. While several different actuation mechanisms could be used to achieve the maneuvers, this section will focus on the use of distributed piezoelectric or electromagnetic linear actuators to strain panels in ways that produce these motions. This architecture has no sliding contact elements (e.g., bearings), and hence has fewer modes of failure. Figure 4 illustrates how the deployable structure (depicted as a simple panel in this case) could be strained using distributed actuators embedded in the frame of the solar panels to produce the desired motions depicted in Fig. 1.

To realize the behavior depicted in Fig. 4, we propose an example actuator mechanism utilizing piezoelectric elements. This

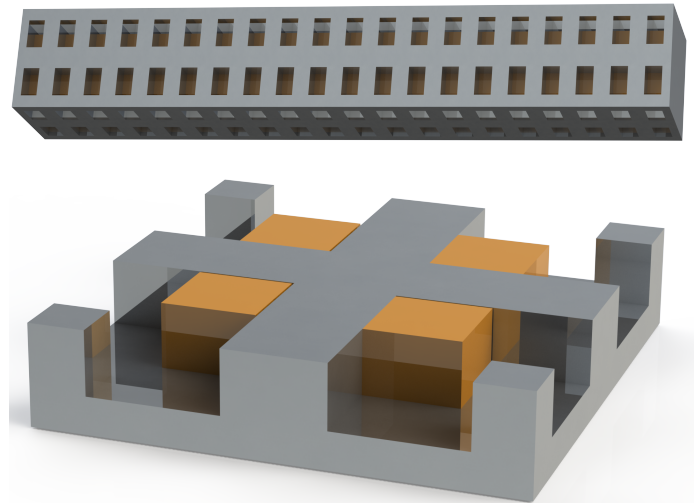


FIGURE 5: Detailed actuator design to produce the motion described in Fig. 1 (above). The cut section of the distributed actuator design (below), with arrangements of piezoelectric elements (orange) to produce bending about any direction, as well as axial extension.

form, illustrated in Fig. 5, is different from that of a solar array, but is helpful for initial conceptual description and analysis. The actuator consists of piezoelectric elements embedded in a metallic bar. The bar is strained in the longitudinal direction by actuating the piezoelectric elements. Some types of piezoelectric actuators can achieve both extension and contraction via different modes of actuation. The actuator in Fig. 5 is used for the dynamic Finite Element Analysis (FEA), and is based on piezoelectric elements manufactured by Physik Instrumente (PI). The specific actuator is known as the ‘PI chips actuator’ [13, 14], and it can be used for extension only (not contraction). To produce bending, two adjacent piezoelectric elements are actuated (elongated), while the opposing two elements remain unactuated. An extension is produced by actuating all four piezoelectric elements. To discuss both bending and extension, we group any two adjacent piezoelectric elements as “Actuator 1” and the remaining two as “Actuator 2”.

4.2 Actuator FEA

The piezoelectric devices chosen are capable of producing a peak force of 200 N [13, 14]. The simulation assumes an open loop bang-bang actuation of the piezoelectric elements, with time steps of 1ms, and a time horizon of 10 ms. The material properties for the metal substrate were chosen as “Aluminium 6061-T4” provided in the SolidWorks catalog. This control strategy was chosen to produce a proof of concept; ongoing work is being conducted to investigate more sophisticated control strategies.

The actuator under analysis can be seen in Fig. 6. The actu-

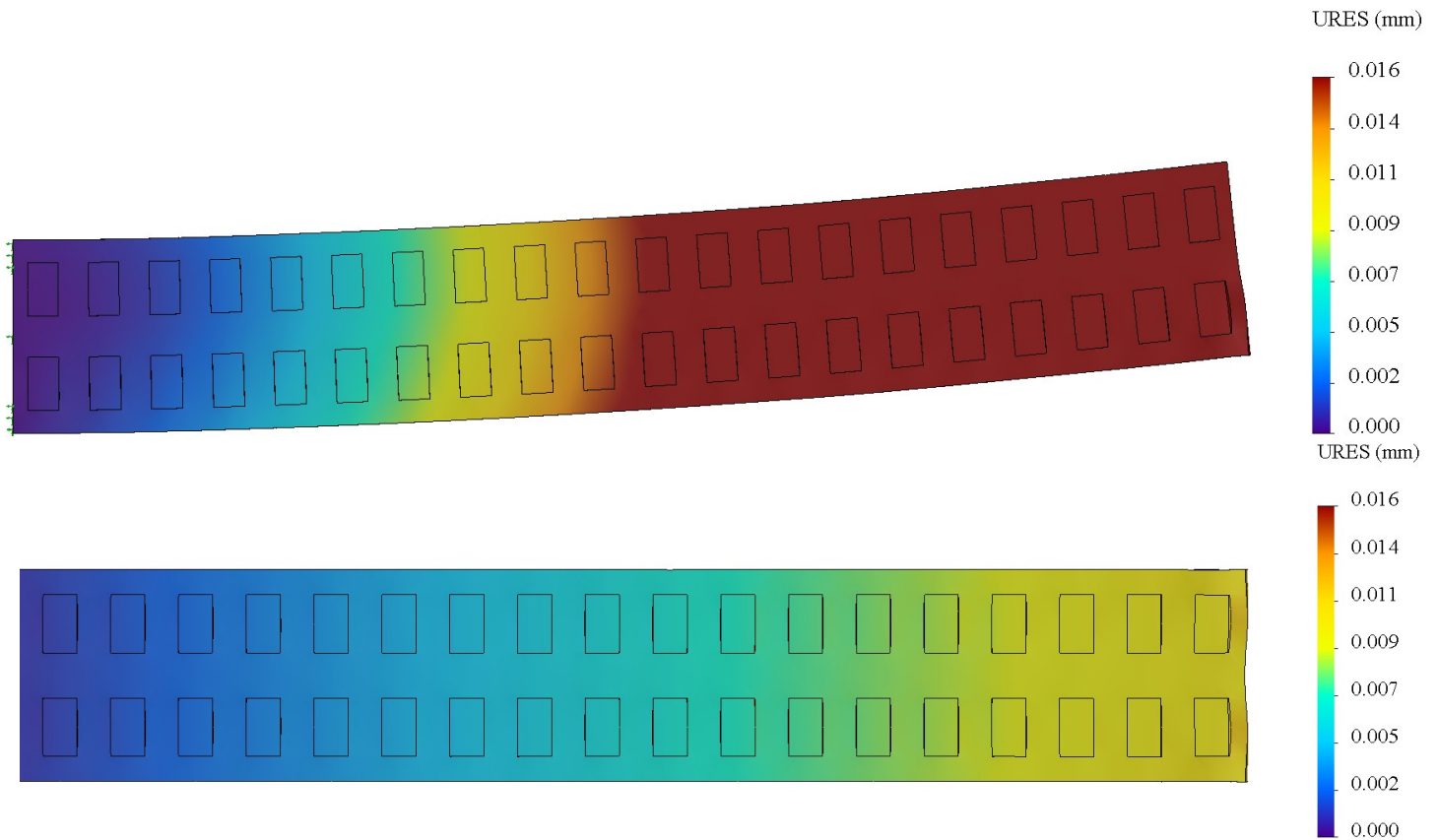


FIGURE 6: Actuator FEA analysis deflections for two deflection modes: shear deflection (top), and linear extension deflection (bottom), the deflections are magnified by a factor of 200.

ator is assumed to have fixed support along the left edge, seen as green arrows (bending case) in Fig. 6.

Figure 6 also shows the physical deformation of the actuator for the two modes. It illustrates both bending and extension modes, along with the corresponding control trajectories. Bending is produced by actuating two adjacent rows of piezoelectric elements (Fig. 5, top), while extension is achieved by actuating all piezoelectric elements, similar to the illustration in Fig. 4. The ‘Resultant nodal displacement’ is plotted in Fig. 7, which is an average across all nodal displacements in the mesh. This result corresponds to uniform piezoelectric elements forces of 200 N. As seen from the FEA results, the maximum extension achieved is on the order of 0.1% of the initial length. The structure oscillates after application of a step input from the piezoelectric elements, indicating that the system can actuate at faster frequencies. Since the natural frequencies are approximately four times higher than the actuation frequency, it is anticipated that the system could be actuated at 4 kHz without any loss in capabilities.

4.3 Amplified actuators

The deflection performance of the piezoelectric actuators can be improved using a compliant mechanism based on a class 2 mechanical lever. Such a mechanism can provide in excess of 1% extension. One such actuator is shown in Fig. 8. The mechanism can amplify the deflection and extension by a factor of 50, while reducing the force at the lever output by the same factor. Since the compliant mechanism will have higher stresses than the simple piezoelectric actuator design, the metal substrate chosen for this case was ANSI-4030 steel. The exact same piezoelectric elements were used so that fair comparison could be made regarding mechanism deflection performance. The bending mode is produced by actuating one of the piezoelectric elements, while an extension is produced by actuating both. Hence, for this actuator design, one of the piezoelectric elements is referred to as “Actuator 1”, while the other one is termed “Actuator 2”.

4.4 Amplified actuator FEA

For the FEA analysis, the mechanism is assumed to have a fixed support along the bottom edge seen as green arrows in Fig. 9. Similar to the simple actuator case, the mechanism is

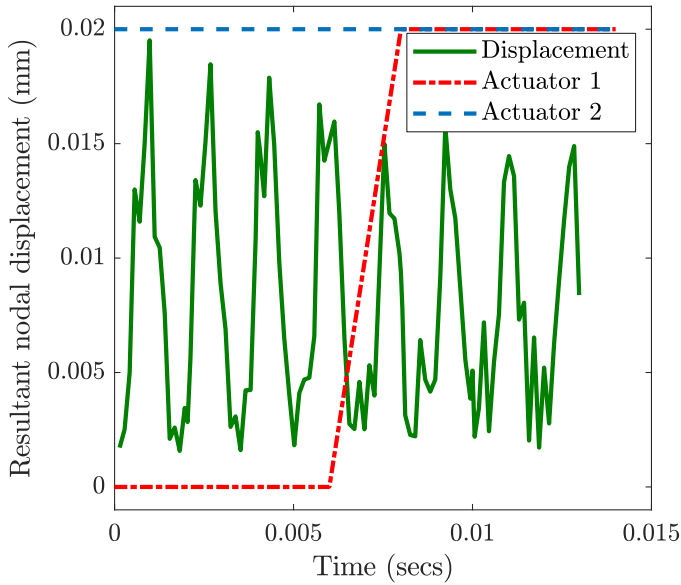


FIGURE 7: Resultant averaged nodal displacement of finite elements during dynamic simulation of the proposed piezoelectric actuator (green solid line). Blue and red dashed lines are normalized to axis limits, and illustrate the control trajectory for two groups of piezoelectric actuators.



FIGURE 8: Piezoelectric actuator with compliant mechanism to amplify deflection, based on a simple class 2 lever mechanism.

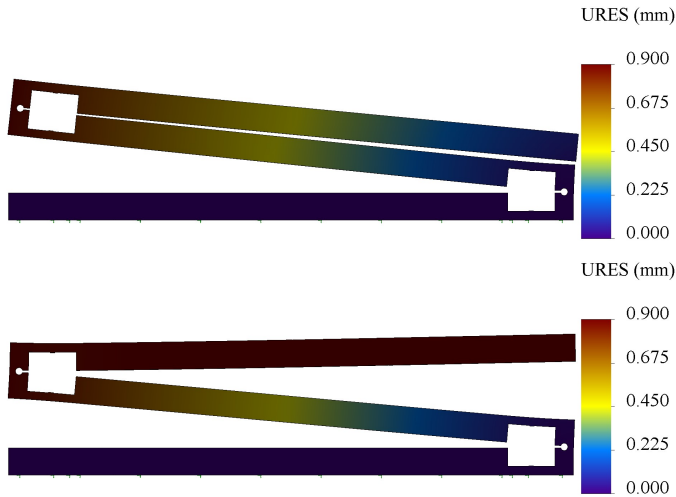


FIGURE 9: Actuator FEA analysis deflection plots for two deflection modes: bending deflection (top), and linear extension deflection (bottom), the deflections are magnified by a factor of 5.

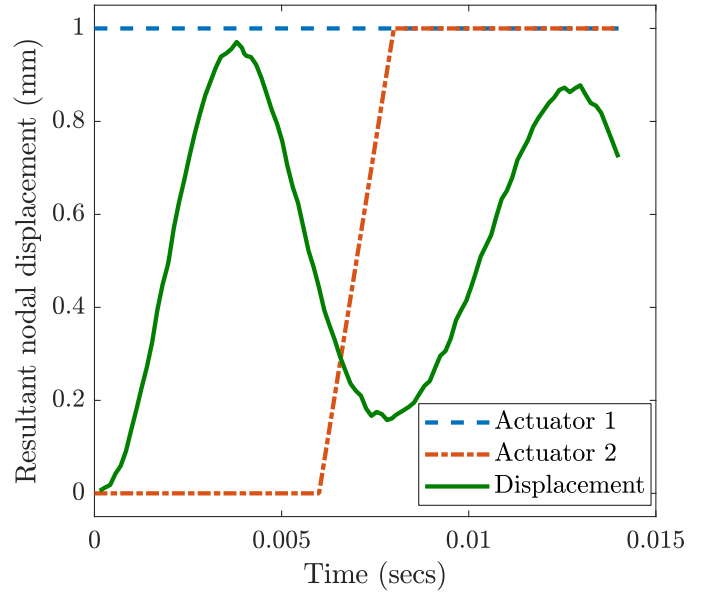


FIGURE 10: Resultant nodal deformation of finite elements during dynamic simulation of the piezoelectric actuator with compliant mechanism amplifier. Blue and red dashed lines are normalized to axis limits, and illustrate the control trajectory for two groups of piezoelectric actuators. Bending mode is followed by extension mode.

assumed to be unstressed but with a bang-bang force profile as seen in Fig. 10. The peak deflections for bending and extension of the proposed actuator can be seen in Fig. 9. This mechanism was tested at maximum extension to determine whether failure of the compliant mechanism might occur. Figure 11 illustrates the von Mises stress at the maximum extension. The arrow in the color bar indicates yield strength, the scale of the color bar has been chosen that any element near or beyond the yield strength will be red colored. It can be seen in Fig. 11 that peak stress is around the circular reliefs, with peak stress of $5.8 \times 10^8 N/m^2$ the actuator assembly does not exceed the yield strength. The peak stress can be seen in the detailed view in Fig. 11.

The resultant nodal displacement from the dynamic FEA simulation is shown in Fig. 10. The response of this system is significantly slower than the previous design, and hence, 1 KHz is close to the natural frequency. While this system is capable of larger strains, it cannot be actuated at higher frequencies unless the mechanical scaling factor is reduced to increase stiffness. This illustrates a fundamental design trade-off between displacement and frequency for the mechanically-amplified actuator, which can be influenced by the mechanical scaling factor.

As seen from this initial analysis, the stiffer mechanism can be faster, but the amplified system is capable of larger displacements. The overall system performance, quantified here as the net satellite rotational velocity (ω_γ) in Eqn. (7), is affected by both by the speed of actuation and by the maximum available

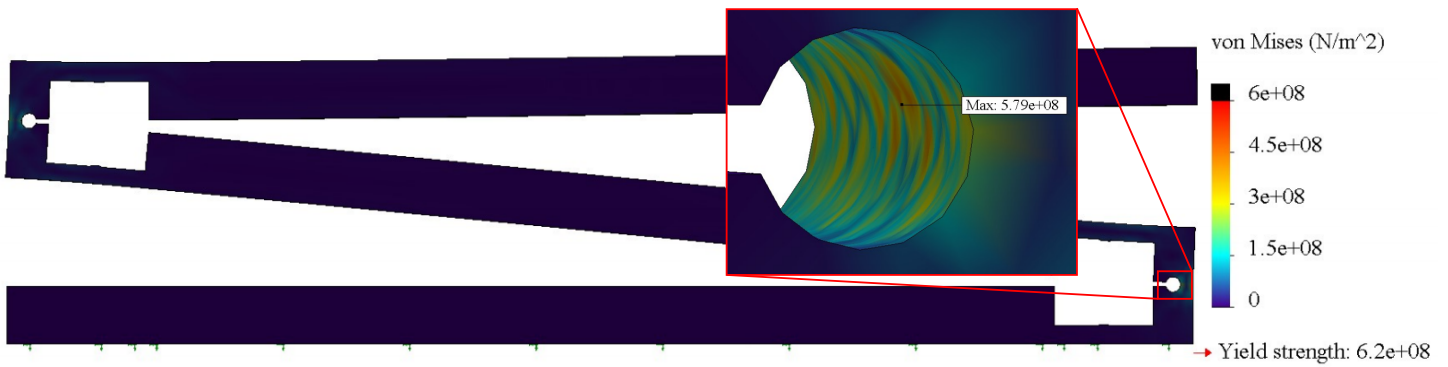


FIGURE 11: Von Mises stress color plot of a maximally-extended compliant mechanism used to amplify deflection. The magnified view of the circular relief shows the area of peak stress located on the interior wall.

extension/compression displacement. For a uniform panel cross-section, mass moment of inertia increases with the square of the panel length ($I_{rest} = \frac{1}{3}ml^2$, where m is total panel mass). In Eqn. (7), velocities are approximated in a linear manner, and based on this strategy, the relative panel (actuator) velocity may be estimated as:

$$\dot{\theta} \approx \frac{\theta_a + \theta_b}{2\Delta t}$$

In other words, ω_γ depends on l in a quadratic manner, whereas ω_γ is proportional to actuator velocity $\dot{\theta}$. Due to the complex tradeoffs observed between displacement, frequency, panel length, and actuator velocity, maximum ω_γ performance is expected to occur at a solution involving a non-trivial combination of physical and control design. Integrated physical and control system design (co-design) studies will be performed to discover these system architectures, similar to those reported in Ref. [15].

4.5 Multibody analysis

A multibody analysis using the SIMULINK modeling environment within MATLAB is presented in this section. The satellite bus dimensions and properties are based on the SSL-1300 satellite bus [16]. An extension of 1% is assumed with no contraction, resulting in: $I_c = I_{rest}$. A bending strain of 10 degrees from the unstrained position is assumed. These assumptions are based on the quantitative results presented in the previous section. In the simulation, the motions described in Section 3 are performed at a frequency of 1 KHz. The satellite body is simulated according to the dimensions shown in Fig. 12, and mass properties listed in the NASA Rapid Spacecraft Development Office (RSDO) spacecraft catalog [16]. The dimensions of an individual panel can be assumed to be the same as the dimension of the face where it folds onto (2.0 meters \times 3.0 meters). The SSL bus¹ typically fly

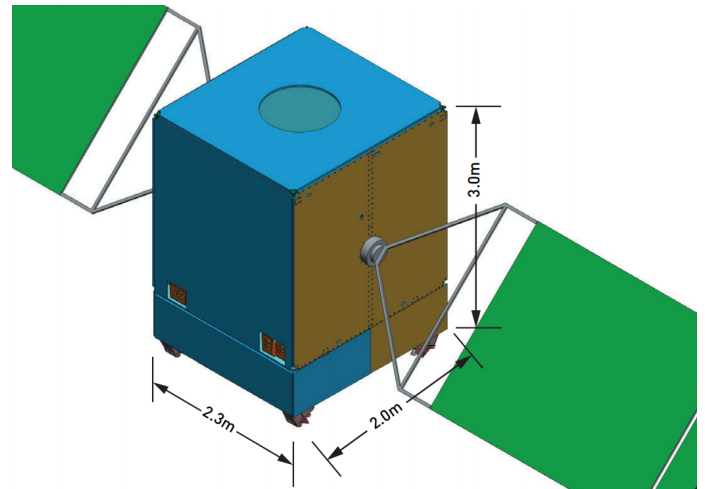


FIGURE 12: Image of SSL1300 bus sizing diagram from NASA Rapid Spacecraft Development Office (RSDO) spacecraft catalog.

Solver type	Variable-step (auto)
Relative tolerance	10^{-8}
Absolute tolerance	Auto
All other settings	defaults

TABLE 2: SIMULINK solver configurations

the four panels in an end-to-end configuration most often, resulting in a deployed panel length of 8 meters on each side.

To ensure that the multibody simulations are accurate, the integrator was employed with the parameters listed in Table 2.

The simulation actuates the panel such that the panels radially extend in the world $X - Y$ plane, and the panels (and consequently) the satellite rotates about the world Z axis, according

¹Bus here refers to the main body of the spacecraft, apart from the MSAC components. In general, the bus may be used to refer to spacecraft product platforms (i.e., elements common across spacecraft variants).

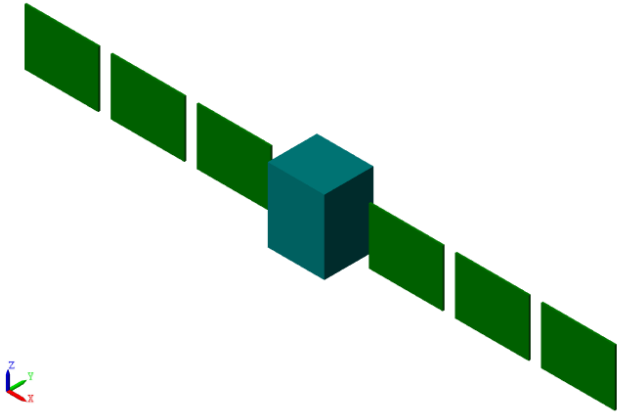


FIGURE 13: Multibody simulation as realized in SIMULINK

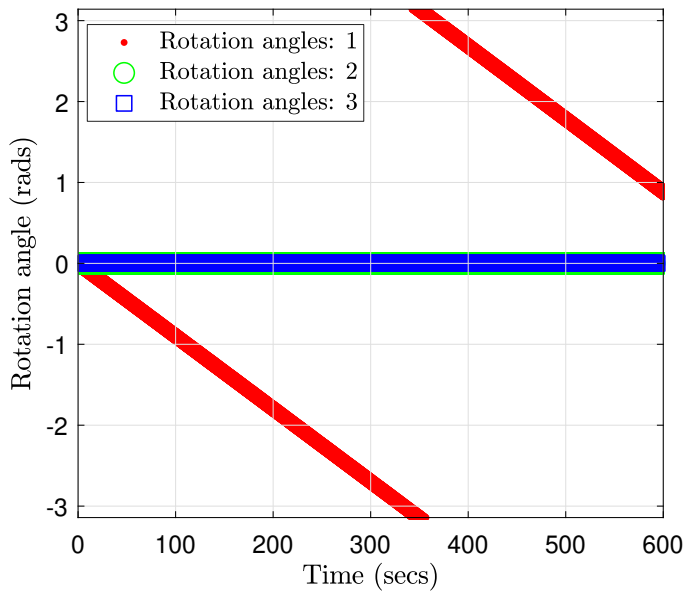


FIGURE 14: Roll, yaw, and pitch of the center body from Fig. 13 for a 600 second simulation of the MSAC system.

to Fig. 13. Figure 14 shows the unfiltered rotation angles for a 600 second simulation. The simulation expresses the rotations as quaternions. The quaternions are then converted to rotation angles. Rotation angle 1 represents the rotation of the satellite about the world Z axis. The discontinuity in the red line in Fig. 14 is due to the rotation angle range $[-\pi, \pi]$.

Figure 15 shows the angular velocity of the satellite body in the world frame. An asymmetric oscillation of about 1 KHz about the Z-axis is observed. Figure 16 shows the angular velocity after applying a low pass digital filter. The filtered signal shows the averaged secular motion generated by the MSAC system, approximated using a SIMULINK. The slope of rotation angle 1 in Fig. 14 agrees to the averaged angular velocity in Fig. 16.

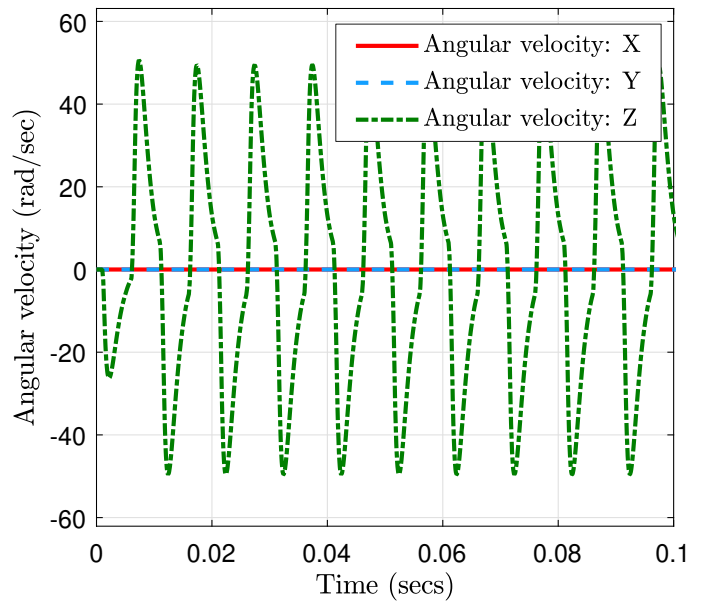


FIGURE 15: Angular velocity of the center body from Fig. 13 for a 600 second simulation of the MSAC system.

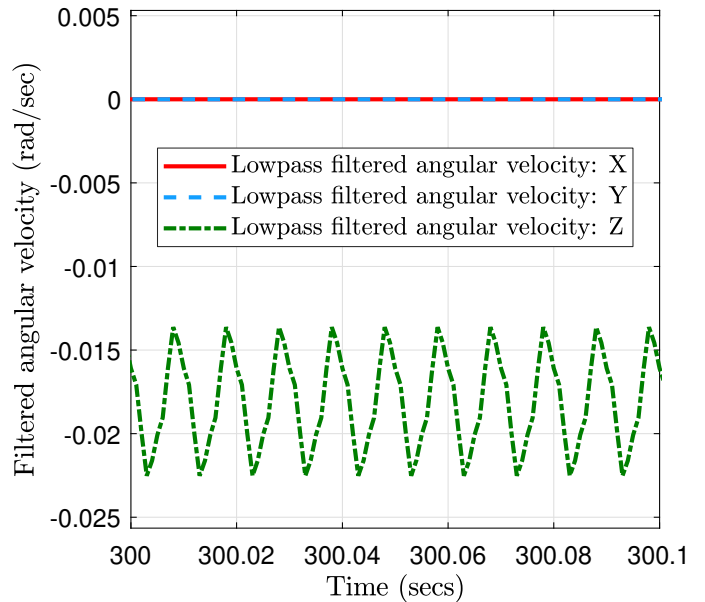


FIGURE 16: Filtered angular velocity of the center body in Fig. 13 for a 600 second simulation of the MSAC system.

5 Future Work

Preliminary modeling and analysis of the MSAC system have been demonstrated in this article. Several design tradeoffs and optimization studies can be carried out to further optimize system performance. Similar trajectories can be achieved using sliding contacts and larger strain actuators, but have been not discussed here due to the mechanical complexity and failure modes

that they introduce. Further aspects that can be altered to improve the system performance is the planform shape of the solar panels, and the use of tensegrity structures to alter the passive dynamic behavior of the deployable panels. The concept also applies to newer class of solar arrays, such as roll-out solar panels, which have been demonstrated in space recently [17].

Alternatively, the conventional passive deployment mechanism of a panel can be modified to be a completely compliant mechanism. The deployment spring loaded hinges can be replaced by compliant revolute joints [18] to reduce the sliding contacts on the mechanism. This will further reduce instances of this important failure mode. This modification will require compliant mechanisms that can withstand very high deformation.

A provisional patent application for MSAC is pending.

6 Conclusion

This paper presents the concept of operation for a novel satellite attitude control system that can produce secular variations to attitude, called Multifunctional Structures for Attitude Control (MSAC). MSAC has similar capabilities as momentum exchange devices, such as control moment gyroscopes and reaction wheel assemblies, and hence can be a replacement for these conventional systems. MSAC, when used as a replacement, can offer mass and volume savings, while reducing spacecraft failure modes. The piezoelectric based MSAC also has the benefit of not having any magnetic interactions with other systems onboard the spacecraft.

7 Acknowledgements

This material is based upon work partially supported by the National Science Foundation under Grant No. CMMI-1653118.

References

- [1] Hemmati, H., 2006. *Deep space optical communications*, Vol. 11. John Wiley & Sons.
- [2] Acton, D. S., Atcheson, P. D., Cermak, M., Kingsbury, L. K., Shi, F., and Redding, D. C., 2004. "James webb space telescope wavefront sensing and control algorithms". In *Optical, Infrared, and Millimeter Space Telescopes*, Vol. 5487, International Society for Optics and Photonics, pp. 887–897.
- [3] Meza, L., Tung, F., Anandkrishnan, S., Spector, V., and Hyde, T., 2005. "Line of sight stabilization of james webb space telescope".
- [4] McNamara, P., Vitale, S., Danzmann, K., Team, L. P. S. W., et al., 2008. "Lisa pathfinder". *Classical and Quantum Gravity*, **25**(11), p. 114034.
- [5] Larson, W. J., and Wertz, J. R., 1992. *Spacecraft subsystems. in: Space mission analysis and design*. Tech. rep., Torrance, CA (United States); Microcosm, Inc.
- [6] Harland, D. M., and Lorenz, R., 2007. *Attitude control system failures. In: Space Systems Failures disasters and rescues of satellites, rocket and space probes*. Springer Science & Business Media.
- [7] Alvarez-Salazar, O. S., Aldrich, J. B., Allison, J. T., and Chung, S.-J., 2016. "Strain actuated solar arrays for precision pointing of spacecraft". In *2016 AAS Guidance, Navigation, and Control Conference*.
- [8] Chilam, C. M., Herber, D. R., Nakka, Y. K., Chung, S.-J., Allison, J. T., Aldrich, J. B., and Alvarez-Salazar, O. S., 2017. "Co-design of strain-actuated solar arrays for spacecraft precision pointing and jitter reduction". *AIAA Journal*, **55**(9), Sept., pp. 3180–3195.
- [9] Herber, D. R., McDonald, J. W., Alvarez-Salazar, O. S., Krishnan, G., and Allison, J. T., 2014. "Reducing spacecraft jitter during satellite reorientation maneuvers via solar array dynamics". In *15th AIAA/ISSMO Multidisciplinary Analysis and Optimization Conference*, p. 3278.
- [10] Coverstone-Carroll, V., and Wilkey, N., 1995. "Optimal control of a satellite-robot system using direct collocation with non-linear programming". *Acta Astronautica*, **36**(3), pp. 149–162.
- [11] Cerven, W. T., and Coverstone, V. L., 2001. "Optimal reorientation of a multibody spacecraft through joint motion using averaging theory". *Journal of Guidance, Control, and Dynamics*, **24**(4), pp. 788–795.
- [12] Reaction/momentum wheel. <https://spinoff.nasa.gov/spinoff1997/t3.html>. Accessed: 2019-04-09.
- [13] Low-voltage piezoelectric chips. https://www.thorlabs.com/newgrouppage9.cfm?objectgroup_id=7563. Accessed: 2019-04-09.
- [14] PICMA chip actuators. <https://www.pi-usa.us/en/products/piezo-actuators-stacks-benders-tubes/pl0xx-picma-chip-actuators-100800/>. Accessed: 2019-04-09.
- [15] Herber, D. R., and Allison, J. T., 2017. "Unified scaling of dynamic optimization design formulations". In *2017 ASME International Design Engineering Technical Conferences*.
- [16] NASA Rapid Spacecraft Development Office (RSDO). <https://rsdo.gsfc.nasa.gov/>. Accessed: 2019-04-09.
- [17] Roll-Out Solar Array (ROSA). https://www.nasa.gov/mission_pages/station/research/experiments/2139.html. Accessed: 2019-04-16.
- [18] Machekposhti, D. F., Tolou, N., and Herder, J., 2015. "A review on compliant joints and rigid-body constant velocity universal joints toward the design of compliant homokinetic couplings". *Journal of Mechanical Design*, **137**(3), p. 032301.